

Modeling the Dynamics of Sub-Millisecond Electroadhesive Engagement and Release Times

Ahad M. Rauf¹ and Sean Follmer¹

Abstract—Electroadhesion is an electrically controllable switchable adhesive commonly used in soft robots and haptic user interfaces. It can form strong bonds to a wide variety of surfaces at low power consumption. However, electroadhesive clutches in the literature engage to and release from substrates several orders of magnitude slower than a traditional electrostatic model would predict, limiting their usefulness in high-bandwidth applications. We develop a novel electromechanical model for electroadhesion, factoring in polarization dynamics and contact mechanics between the dielectric and substrate. We show in simulation and experimentally how different design parameters affect the engagement and release times of electroadhesive clutches to metallic substrates. In particular, we find that higher drive frequencies and narrower substrate aspect ratios enable significantly faster dynamics. We demonstrate designs with engagement times under 15 μs and release times as low as 875 μs , which are 10 \times and 17.1 \times faster, respectively, than the best times found in prior literature.

Index Terms—Electroadhesion, switchable adhesion, dynamics, modeling, actuators

I. INTRODUCTION

Switchable adhesives can dynamically adhere to and release from contacting surfaces. They are widely used in soft robots, haptic interfaces, and biomedical devices, with applications in robotic grippers [1, 2], wall climbing and perching robots [3, 4], exoskeletons [5, 6], haptic user interfaces [7-10], and kinesthetic garments [11, 12]. Different switchable adhesion mechanisms can be compared by their shear force capacity when gripping different substrates and by their engagement and release speeds [13]. Mechanisms with high shear force capacities, like granular jamming actuators and shape memory polymers, often require long switching times due to viscoelastic effects, while faster adhesives like liquid crystal elastomers and gecko-inspired adhesives often have caveats like low force capacity or poor adhesion to rough surfaces [14, 15].

Electroadhesion (EA), or the electrostatic attraction between two contacting materials separated by a dielectric and held at a potential difference, has emerged as an effective electrically triggered switchable adhesive. Its scalable manufacturing process, high shear force capacity against a wide range of substrates, relatively fast actuation speeds, low power consumption, and low profile have made EA useful for space- and power-constrained applications. In this paper, we focus on a common implementation, shown in Fig. 1, where one of the contacting materials is a dielectric patterned with interdigitated

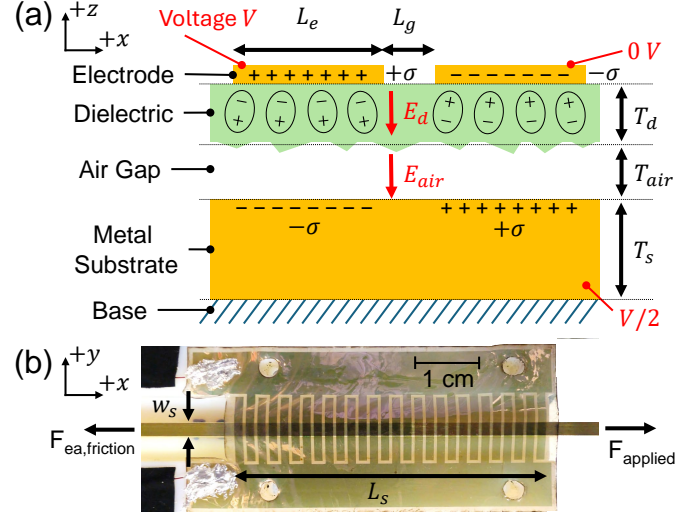


Fig. 1. (a) Schematic diagram and (b) picture of an electroadhesive clutch. When a voltage V is applied, the polarization of bound charges in the dielectric amplifies the field strength, attracting the film to the metal substrate. The resulting friction can counteract applied shear loads on the substrate.

comb electrodes while the other contacting material can be any conductive or insulating substrate. This form factor, originally developed in 1968 by Krape [16], sacrifices some adhesive force capacity compared to a parallel plate configuration in which both contacting materials have electrodes. However, EA with Interdigitated Co-planar Electrodes (shortened to EA-ICE in this paper) allow all the electronics to be concentrated into a single surface, reducing bulk and enabling the clutch to adhere to small, delicate objects and generic surfaces in the field.

Despite its widespread utility, there is a lack of accurate dynamics models for how quickly EA pads can adhere to and release from surfaces. Prior work has shown that the dielectrics themselves can be charged and discharged on the order of microseconds [17, 18]. However, as shown in Fig. 2, every paper we found reported engagement times from hundreds of microseconds to milliseconds and release times ranging from tens of milliseconds to minutes. While some models predicting minute-scale release times have been proposed (although, to our knowledge, never compared numerically against experimental data) [19-22], experimental results in the microsecond to millisecond range have largely gone unexplained, limiting EA's scalability to high-bandwidth applications [10, 23]. Slow dynamics also leads to “stick-slip” behavior, where after an applied load exceeds an EA clutch's force capacity the clutch slips, losing up to 70% of its frictional capacity and requiring tens of milliseconds to re-engage [6, 24]. In this paper, we

This work is supported by the National Science Foundation CAREER award grant no. 2142782.

¹ Authors are with the Department of Mechanical Engineering at Stanford University, Stanford, CA 94305, USA. ahadrauf@stanford.edu

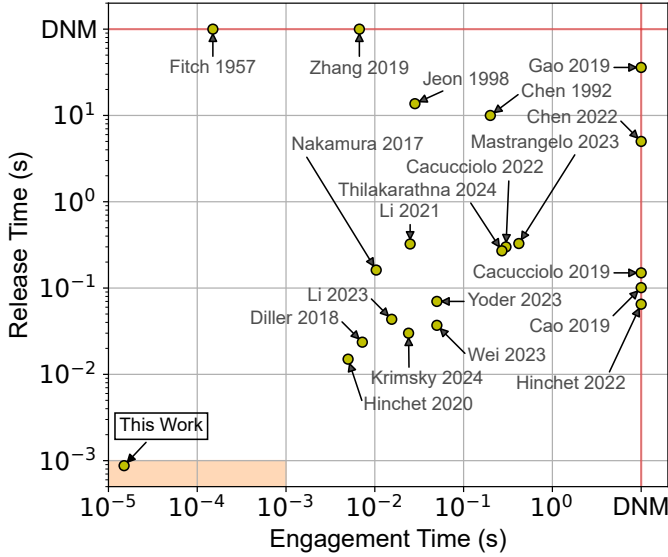


Fig. 2. Comparison of engagement and release times of centimeter-scale EA clutches in the literature. Papers that did not report one of the two metrics are placed on the red “Did Not Measure” (DNM) axis. The orange highlighted area indicates sub-millisecond engagement and release times.

aim to understand and model this literature gap, opening optimization potential for EA pads to serve as ultra-fast, electrically controllable, planar adhesive clutches.

We developed an electromechanical EA dynamics model, factoring in the dynamics of the drive circuitry, polarization, and mechanical contact between the EA pad and substrate. We test using simulation and experiments how different geometric and operating parameters affect the EA clutch’s engagement and release times to metallic substrates when loaded in shear. We demonstrate EA clutches with engagement times under 15 μ s and release times as low as 875 μ s, which are 10 \times and 17.1 \times faster, respectively, than the best times found in prior literature. We anticipate these results can be used to optimize EA clutches for high-bandwidth switchable adhesion applications, such as haptic interfaces, wearable robots, and biomedical devices.

II. MODELING ELECTROADHESION

We first modeled the electrical and mechanical dynamics separately to understand the relevant design variables, and then combined them into a full electromechanical dynamics model. While our derivations focus on EA-ICE clutches, the final equations are almost identical for parallel plate EA clutches.

A. Quasistatic Electrostatic Force

As shown in Fig. 1, we consider an interdigitated comb pattern of N electrodes, each with length L_e and spaced L_g apart. The EA pad is attracted to a substrate of length L_s , width w_s , and thickness T_s . The dielectric thickness is T_d , its relative permittivity is κ , and the average air gap is T_{air} . We assume a metal substrate to facilitate modeling, as discussed further in Sec. II-B. Fig. 1(a) shows a diagram of the layer stack’s electric fields and charge densities. After depositing a surface charge density σ on an electrode of area $A = L_e w_s$, a charge

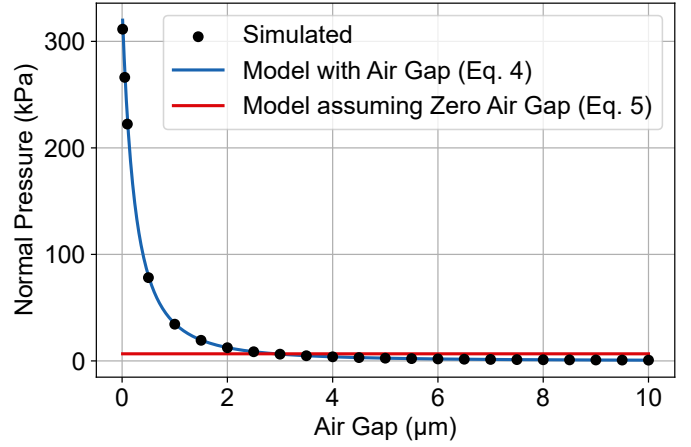


Fig. 3. Comparison of the normal EA force predicted by a finite element simulation against the analytical models in Eq. 4 and Eq. 5.

TABLE I
ELECTROADHESIVE CLUTCH AND SUBSTRATE DIMENSIONS

N	28
L_e (mm)	1.5
L_g (mm)	0.5
T_d (μ m)	24
L_s (mm)	55.5
$w_s \times T_s$ (mm \times mm)	2×2 ; 2.5×2.5 ; 3×3 4×2 ; 5×2.5 ; 6×3

$-\sigma$ is induced in the substrate. Inspired by Nakamura and Yamamoto [20], the capacitance between each electrode and the substrate can be modeled as a dielectric and air capacitor in series. The capacitance between N adjacent electrodes (half held at potential V , half at ground) is thus:

$$C = \frac{N\kappa\epsilon_0 A}{4(T_d + \kappa T_{air})} \quad (1)$$

Rearranging this equation, we can estimate the air gap via:

$$T_{air} = \frac{N\epsilon_0 A}{4C} - \frac{T_d}{\kappa} \quad (2)$$

The electric fields in the dielectric and air are $E_d = \frac{\sigma}{\kappa\epsilon_0}$ and $E_{air} = \frac{\sigma}{\epsilon_0}$, respectively. Because the metal substrate is left floating, its effective potential is $V/2$. This potential difference can be related to the electric fields and charge densities by:

$$\frac{V}{2} = E_d T_d + E_{air} T_{air} = \sigma \left(\frac{T_d}{\kappa\epsilon_0} + \frac{T_{air}}{\epsilon_0} \right) \quad (3)$$

The normal force on the substrate from an electroadhesive pad with N electrodes is thus:

$$F_{ea}(T_{air}) = \frac{\sigma N A E_{air}}{2} = \frac{\kappa^2 \epsilon_0}{2} \frac{N A (V/2)^2}{(T_d + \kappa T_{air})^2} \quad (4)$$

Eq. 4 differs from a conventional parallel plate force derivation that ignores the effect of the air gap [7, 36]:

$$F_{e,s,T_{air}=0} = \frac{\kappa\epsilon_0}{2} \frac{N A (V/2)^2}{T_d^2} \quad (5)$$

While the air gap’s importance is well-established empirically in the literature for designing high-force EA clutches [36], Eq. 4 helps explain why. As depicted in Fig. 1(a), the

polarized dielectric's bound charge amplifies the air's electric field by an extra factor κ , enabling higher forces for very small air gaps. To verify our model, we developed an electrostatics finite element simulation in Altair Flux for an EA-ICE clutch with nominal dimensions (Table I), a 2 mm wide metal substrate, and a 5 μm air gap. Fig. 3 compares the simulated normal pressure against Eq. 4 and Eq. 5, showing that Eq. 4 well approximates the finite element simulation to within 3%.

While we leave a full retrospection to future work, we propose that factoring in the air gap via Eq. 4 can enable better predictions of EA clutch performance. For example, Hinchet and Shea [12] measured a capacitance of $0.76 \frac{nF}{\text{cm}^2}$ for a parallel plate EA clutch at 150 V, which corresponds to an air gap of 610 nm (Eq. 2) and a predicted shear force capacity of 73.9 kPa (Eq. 4). This is much closer to their measured 79.2 kPa than Eq. 5's predicted 7.2 kPa. Similarly, Berdozzi et al. [37] measured a capacitance change of 76.9 pF for an EA-ICE clutch at 1 kV, corresponding to an air gap of 9.2 μm . Eq. 4 predicts a much closer shear force capacity of 2.54 kPa to their measured 2.02 kPa than Eq. 5's predicted 15.3 kPa. Diller et al. [6] also noted in their analysis that their data fits κ^2 much better than the κ they were using from Eq. 5.

B. Extending Quasistatic Analysis to the Transient Domain

In this section, we extend the quasistatic analysis in Sec. II-A to the transient domain, considering how polarization dynamics and the high voltage drive circuitry could affect EA dynamics. Contrary to some assertions in prior work [19, 20], we conclude that the upper limit of EA dynamics will be limited largely by mechanical rather than electrical dynamics.

1) *Dielectric Constant Dynamics:* Sec. II-A's quasi-static analysis assumed that the substrate's induced charge instantaneously matches the deposited surface charge σ . On our time scale, this works for our metal substrate, in which charges can migrate in under a nanosecond. However, dielectrics move charges more slowly as polymer chains and interfacial charges reorient to be in line with the electric field [19].

A dielectric's relative permittivity can be written as a function of angular frequency ω using the Cole-Cole equation:

$$\kappa(\omega) = \kappa_\infty + \frac{\kappa_s - \kappa_\infty}{1 + (j\omega\tau)^\alpha} \quad (6)$$

where κ_∞ is the high-frequency limit of the relative permittivity, κ_s is the low-frequency saturated relative permittivity, τ is the characteristic relaxation time, and $0 \leq \alpha \leq 1$ describes the broadness of the dielectric dispersion spectra.

In this paper, we focus on the dielectric and relaxor ferroelectric P(VDF-TrFE-CFE) (poly(vinylidene fluoride-trifluoroethylene-chlorofluoroethylene)), which is commonly used in EA clutches in the literature for its high breakdown field and permittivity [7, 30]. Modeling the charge as a step input, we can take the inverse Laplace transform:

$$\kappa(t) = \kappa_\infty \delta(t) + (\kappa_s - \kappa_\infty) \left(\frac{t}{\tau}\right)^\alpha E_{\alpha, \alpha+1} \left(-\left(\frac{t}{\tau}\right)^\alpha\right) \quad (7)$$

where $\delta(t)$ is the Dirac delta function and $E_{\alpha, \beta}(z)$ is the Mittag-Leffler function. Fig. 4 shows the step input response to a fitted Cole-Cole model for P(VDF-TrFE-CFE) based on

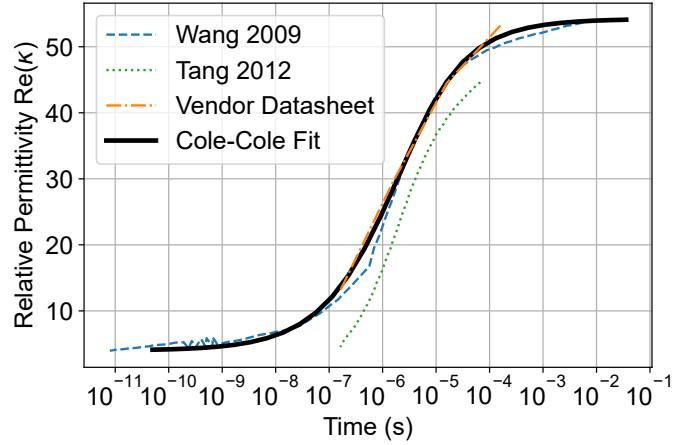


Fig. 4. Step input response of a Cole-Cole dielectric constant model for P(VDF-TrFE-CFE). The model was least squares fit to experimental data from three sources, each measured across different frequency domains.

data from our vendor datasheet and from [17, 18], which tested samples with a similar composition and annealing process to our own. Taking $\kappa_\infty = 4$ based on [17], the best fit coefficients were $\kappa_s = 54.2$, $\tau = 2.82 \mu\text{s}$, and $\alpha = 0.562$. Interpreting the graph, after a charge σ is deposited on (or removed from) an electrode, the dielectric can reach 93% polarization (or depolarization) within the first 100 μs . Similar curves can be drawn for other common EA dielectrics, and we conclude that while polarization dynamics set an important upper threshold on EA bandwidth, they are not primarily responsible for the 5-50 ms engagement times seen in prior literature (Fig. 2).

An important note is that the Cole-Cole model applies when the EA pad is driven by a power supply that can both source and sink charge. Prior modeling literature often asserts, based on the language for Maxwell-Wagner interfacial polarization, that the characteristic relaxation time should be on the order of seconds to minutes [19-21]. However, this assumes the EA pad is disconnected from a power supply and thus can only dissipate charge through internal resistance and stochastic depolarization. Although this is useful in applications such as perching robots, we proceed with the Cole-Cole model since most EA devices always stay connected to their power supply.

2) *High Voltage Drive Circuit Dynamics:* The output resistance of the high voltage drive circuit is also important to consider when modeling EA dynamics. Output stages include common source amplifiers [7, 8], push-pull output stages such as half bridges [38] and full bridges [11, 12, 24, 39], and optocoupler relays [6, 15]. Although the transistors in these circuits have response times far faster than EA's mechanical time constants, many small form factor DC-DC converters cannot handle the large current spikes that occur whenever these transistors flip on or off. Several previous papers thus use M Ω -scale current-limiting resistors in series with their EA clutches, which we believe plays a large role in why they cite millisecond-scale rise and fall times for their high voltage drive circuits [7, 39]. We expect that pairing a high voltage amplifier capable of handling these current spikes together with a fast output stage can enable better engagement and release times.

C. Mechanical Dynamics

Until now, we have assumed the dielectric and substrate's surfaces are perfectly flat. However, as shown in Fig. 1(a), the interface between an EA pad and substrate has many random asperities. As the asperities compress against each other, the apparent contact area between the two surfaces increases, resulting in what classical mechanics calls "normal force" [40].

We consider a simplified surface profile, where the average gap between the surfaces is T_{air} and the distribution of asperities heights is Gaussian with standard deviation σ_d . Greenwood and Williamson's contact mechanics model [41], which is prevalent in tribology theory, models the stiffness force between a rigid substrate and deformable surface as:

$$F_k(T_{air}) = kL_s w_s \sigma_d^{1.5} G_{1.5} \left(\frac{T_{air}}{\sigma_d} \right) \quad (8)$$

where k is a fitted parameter related to the asperity geometry and material parameters. $G_{1.5}(h)$ is a function with the form:

$$G_{1.5}(h) = \frac{\sqrt{h} e^{-\frac{h^2}{4}}}{4\sqrt{\pi}} \left[(h^2 + 1) K_{\frac{1}{4}} \left(\frac{h^2}{4} \right) - h^2 K_{\frac{3}{4}} \left(\frac{h^2}{4} \right) \right] \quad (9)$$

where $K_\nu(z)$ is the Basset function. $G_{1.5}(\frac{T_{air}}{\sigma_d}) \approx 0.43$ when $T_{air} \ll \sigma_d$, and quickly drops off to zero once $T_{air} > \sigma_d$.

Because of the large area and small gap, the film will likely experience squeeze-film damping as its predominant form of viscous damping. Griffin et al. [42] derived a first-order approximation for large flat plates:

$$F_b(T_{air}) = \left(\frac{96\mu \min(L_s, w_s)^3 \max(L_s, w_s)}{\pi^4 T_{air}^3} \right) \dot{T}_{air} \quad (10)$$

where $\mu = 18.5 \mu\text{Ns/m}^2$ is air's dynamic viscosity. To account for the Gaussian distribution of asperity heights, we can find the average damping force by integrating $F_b(T_{air})$ with the asperity height's probability density function [43]:

$$F'_b(T_{air}) = \int_0^\infty F_b(\tau_{air}) \left(\frac{e^{-(T_{air}-\tau_{air})/2\sigma_d^2}}{\sigma_d \sqrt{2\pi}} \right) d\tau_{air} \quad (11)$$

We can similarly define F'_{ea} :

$$F'_{ea}(T_{air}) = \int_{-\frac{T_d}{\kappa}}^\infty F_{ea}(\tau_{air}) \left(\frac{e^{-(T_{air}-\tau_{air})/2\sigma_d^2}}{\sigma_d \sqrt{2\pi}} \right) d\tau_{air} \quad (12)$$

where the negative integral range accounts for when the dielectric compresses against asperities. These alterations have very little effect when $T_{air} \gg \sigma_d$, but for our nominal T_d it can increase F_{ea} by up to $11.1\times$ when $T_{air} \approx \sigma_d$.

D. Full Electromechanical Dynamics Model

Combining the equations from the last three sections together, we can write equations of motion in the z axis for the dielectric and substrate. We assume the substrate is much heavier than the dielectric (i.e., fixed in z -height), while the dielectric is free to move. The dielectric also has a small preload force $F_{preload}$ applied to help prevent wrinkles and ensure even contact between the surfaces. The dielectric's equation of motion along the z axis is:

$$m_d \ddot{T}_{air} = F_k - F'_b - F'_{ea} - m_d g - F_{preload} \quad (13)$$

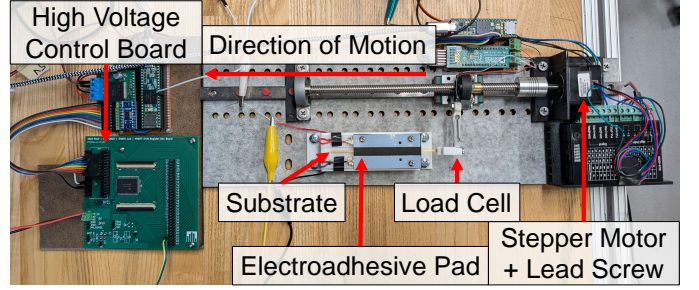


Fig. 5. Experimental test setup for measuring EA shear force as the load cell on a motorized stage pushes against the substrate.

where the first term on the right side comes from contact mechanics (Eq. 8), the second term comes from damping (Eq. 11), the third comes from electrostatics (Eq. 12, but incorporating the rise and fall times of κ and V as described in Sec. II-B), and the fourth comes from gravity on the dielectric mass m_d . The system of equations can be solved for as an initial value problem with the state $[T_{air}, \dot{T}_{air}]$.

The substrate's equation of motion along the z axis is:

$$0 = F_{N,base} + F'_{ea} - F_k + F'_b - m_s g \quad (14)$$

where $F_{N,base}$ is the normal force from the base on the substrate and m_s is the mass of the substrate. Since $F_{N,base}$ does not directly affect the dynamics, we leave it as is instead of modeling its contact mechanics and air gap.

We denote the substrate's coefficients of friction with the dielectric and base as μ_d and μ_{base} , respectively. After solving Eqs. 13 and 14 for T_{air} , we can predict the shear friction on the substrate while the substrate is moving and while the dielectric and base remain fixed along the substrate's axis of motion:

$$F_{shear} = \mu_{base} F_{N,base} + \mu_d F_k \quad (15)$$

Once the gap settles ($\ddot{T}_{air} = 0$) and after solving Eq. 13 for T_{air} , we can predict the EA clutch's shear force capacity:

$$F_{shear,max} = \mu_{base}(m_d g + m_s g + F_{preload}) + \mu_d F_k \quad (16)$$

The preload force can also be estimated by measuring the force $F_{shear,V=0}$ required to push the substrate when $V = 0$:

$$F_{preload} = \frac{F_{shear,V=0} - \mu_{base} m_s g - \mu_d m_d g}{\mu_d + \mu_{base}} \quad (17)$$

III. SHEAR FORCE CAPACITY RESULTS

A. Experimental Setup and Testing Procedure

To test our model, we built the experimental test setup in Fig. 5 to measure the shear force capacity, engagement time, and release time of an EA pad to a metallic substrate across a variety of geometric and operating parameters. Similar to prior work [6, 24], we created a tensile testing machine by mounting a 500g load cell (UXCell, China) on a motorized linear slide. The stepper motor moving the slide block was driven at 1/256 microstepping, and the load cell was sampled at about 12.8 kHz (ADS1263, Texas Instruments, USA). The voltage was sampled on a Teensy 4.1 microcontroller (PJRC, USA) using a 100:1 resistive divider (10.1 M Ω total).

The EA pad was made using a 24 μm thick P(VDF-TrFE-CFE) film with 7 mol% CFE and a sputtered gold layer on one side (PolyK Technologies, LLC, USA). An interdigitated electrode pattern with dimensions in Table I was etched into the gold using a quasi-CW DPSS UV laser cutter (Series 3500, DPSS Lasers Inc., USA). Enamelled copper wire was adhered to each electrode using silver conductive epoxy. As shown in Fig. 1(b), the interdigitated electrodes were designed to be wider than the substrate to mimic prior work on using EA clutches to manipulate small metallic objects [8], and to mitigate inconsistencies if the pin slipped sideways when reset between runs. The high voltage drive signal was powered by a 50 mA rated DC-DC converter (AHV12V500V50MAW, Analog Technologies, USA) and a high voltage shift register with a half-bridge output stage (HV507, Microchip Technology Inc., USA). We observed rise times (10% - 90%) of 8.3 μs and fall times of 5.2 μs when the power supply drove our EA pad. We measured an average power consumption of 1.43 mW for a 300 V, 1 kHz bipolar square wave drive signal.

We used six brass substrates (Albion Alloys, England) with different dimensions shown in Table I. Screws were tightened through mounting points in the assembly to lightly press the dielectric into the substrate, which helped reduce film wrinkling under high shear stress. Pressure was evenly distributed along the sides using 3D printed brackets and a 1/16" closed-cell blended EPDM foam (McMaster-Carr Supply Company, USA). The foam was chosen for its low modulus (comparable to 5A durometer silicone) and low tackiness.

The base that the substrate moves on was 3D printed from VeroWhitePlus photopolymer using a Strasys Objet24 V3. To measure the coefficient of friction, we took the ratio between tangential and normal force across 10 trials, measuring $\mu_{\text{base}}^{\text{static}} = 0.281$ and $\mu_{\text{base}}^{\text{kinetic}} = 0.173$ between the brass substrate and the base plate; and $\mu_{\text{d}}^{\text{static}} = 0.188$ and $\mu_{\text{d}}^{\text{kinetic}} = 0.154$ between the substrate and the dielectric film.

Fig. 6 shows a sample experimental run. The stepper motor drives the substrate forward at 0.5 mm/s for 3 sec to establish a baseline kinetic friction force reading. We then turned on the voltage while continuing to drive the motor for 1.5 sec. Finally, the motor is stopped, the voltage is removed, and the load cell is allowed to settle for 2 sec. Load cell readings were filtered through a zero-phase 250 Hz low-pass filter to eliminate background noise, similar to prior work [6].

B. Fitting Contact Mechanics Model

To fit the parameters k and σ_d in Eq. 8, we measured the capacitance of our EA pad against brass substrates of different widths across a range of applied normal forces, as shown in Fig. 7. The EA pad's capacitance was read using a Keysight U1701B capacitance meter, after subtracting parasitic capacitance. The air gap was then estimated using Eq. 2. Fitting the air gap and normal force data to Eq. 8, our best fit parameters were $k = 5.39 \cdot 10^{14} \text{ N/m}^{3.5}$ and $\sigma_d = 2.80 \mu\text{m}$. This method is an accessible alternative to traditional surface profilometry for characterizing EA dielectric surfaces [44].

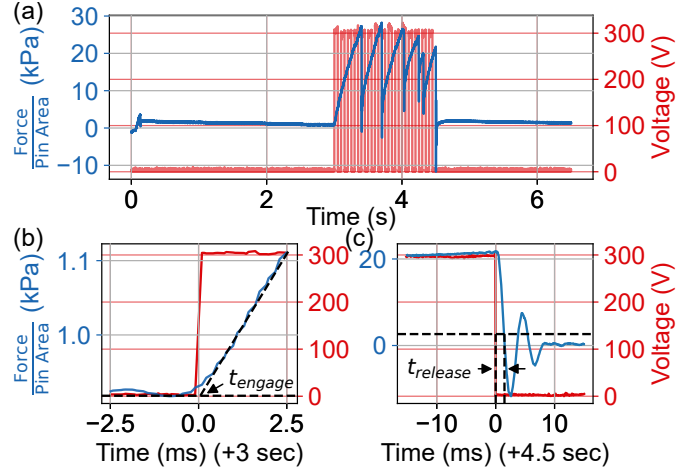


Fig. 6. (a) Load cell force measured over the course of a shear force capacity test. The drive signal, shown for one electrode, was a 300 V, 10 Hz bipolar square wave. (b) Calculation procedure for the engagement time of this sample. The force profile's rounded corner when the voltage rises is due to filtering, so the engagement time is measured when the force profile after the voltage rises linearly interpolates to the average force before the voltage rises (shown via dotted black lines). (c) Calculation procedure for the release time of this sample, measured as the time between when the voltage falls and when the load cell falls to within 10% of its final settling value. Using these metrics, for the sample shown $t_{\text{engage}} = 49.4 \mu\text{s}$ and $t_{\text{release}} = 1.49 \text{ ms}$.

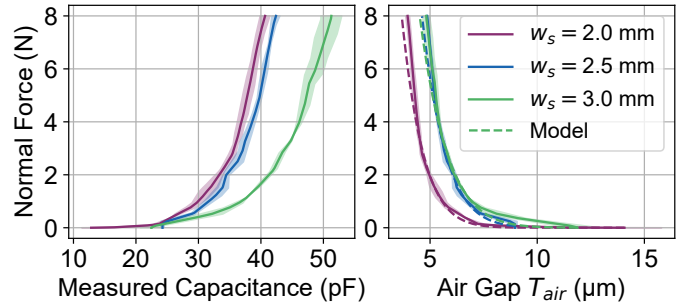


Fig. 7. For a range of applied normal loads, we measured the capacitance and used it to estimate the air gap using Eq. 2. The average and standard deviation across 3 trials is shown.

C. Shear Force Capacity Measurements and Modeling

Although maximizing shear force capacity is not a primary objective of this paper, understanding how different parameters affect our clutch's force capacity can help validate whether our model is physically sound. Fig. 8 shows the measured and predicted (Eq. 16) shear force capacities at different voltages and bipolar square wave AC drive frequencies.

When applying our model, we found that our analytical EA force equation was slightly inconsistent from what was needed to produce the measured shear capacities, so we fitted a multiplier $\lambda_{\text{ea}}^{\text{fit}}(V)$ for F_{ea} to each voltage's curve in Fig. 8:

$$F'_{\text{ea,adj}} = \lambda_{\text{ea}}^{\text{fit}}(V) F'_{\text{ea}} \quad (18)$$

We found that the best fit values followed a roughly linear relationship $\lambda_{\text{ea}}^{\text{fit}}(V) = 2.40 - 0.0058V$ ($R^2 = 0.98$). The average value of $\lambda_{\text{ea}}^{\text{fit}}$ over all samples was 1.08 ($\sigma = 0.33$). Because the average $\lambda_{\text{ea}}^{\text{fit}}$ was about 1 and because the model accurately predicted the shear pressure capacity's decay at high frequencies, we take these results as confirmation that

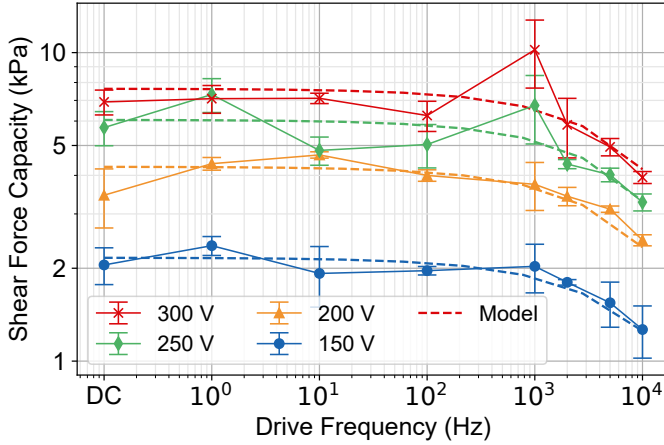


Fig. 8. Shear force capacity measured for a 2 mm wide substrate at different voltages and drive frequencies, averaged over at least 5 trials per condition.

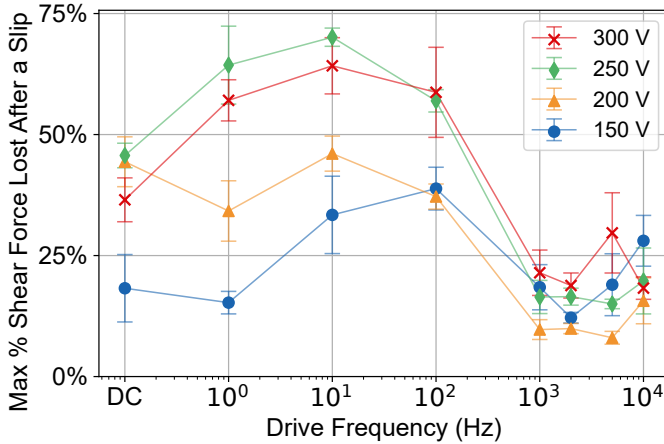


Fig. 9. Max slip percentage measured for a 2 mm wide substrate at different voltages and drive frequencies, averaged over at least 5 trials per condition.

our electromechanical model is physically sound, except for what we hypothesize are unmodeled parasitics.

The -3 dB frequency for all voltages is experimentally over 10 kHz, and is predicted by our model to be about 13.3 kHz. For comparison, Chen et al. [19] measured a -3 dB frequency of about 150 Hz for both square and sine AC drive signals using a glass substrate, Zhang et al. [8] measured a -3 dB frequency of about 130 Hz for sine AC drive signals against a brass metal substrate, and Shultz et al. [10] measured a -3 dB frequency of around 75 Hz for sine AC drive signals using a human fingertip as the substrate. We predict the difference is due largely to the improved dynamics of our drive circuitry and our use of a metal substrate.

D. Force Slip vs. Frequency

As shown in the sample force profile in Fig. 6(a), EA clutches lose a significant amount of their load-carrying capacity after a slip, with similar clutches in the literature often losing 50-70% of their measured force and requiring tens of milliseconds before the clutch re-engages [6, 24]. This failure mode is a major deterrent to using EA clutches in safety-critical robots. Fig. 9 shows how the worst slip in each of our

test runs compares across different voltages and frequencies, measured as the percentage of force lost after the slip. We found that the slip percentage decreases drastically at higher frequencies, with 250 V seeing a $4.7\times$ reduction on average between the 10 Hz and 5 kHz drive frequencies. Our numerical values cannot be compared directly with prior work, since the slip percentage also varies with load cell dynamics, but prior work has primarily used DC up to 10 Hz drive signals. Our hypothesis, which we explore further in Sec. IV, is that higher drive frequencies can enable faster actuation times.

IV. ENGAGEMENT AND RELEASE TIME RESULTS

A. Engagement Time Testing and Simulation Methods

To measure the engagement time, we adapted a method from Diller et al. [6], shown in Fig. 6(b). We linearly interpolated the load cell readings after the voltage is enabled down to the average force over the 10 ms before the voltage is enabled. To minimize the impact of noise, we found linear interpolations for every data interval starting from 0.5 ms after the voltage is enabled and ending between 2-20 ms after the voltage is enabled. After filtering to only fits with $R^2 > 0.8$, we chose the smallest positive interpolated intersection to be the engagement time. For some tests, there would be no positive values due to noise; in these cases, we rounded the run's measured engagement time up to 0.

When using the model to predict engagement time, we solved the initial value problem defined by the coupled equations of motion Eqs. 13 and 14 for T_{air} as a function of time. For each experimental run, we extracted a single piece of information to simulate its dynamics, estimating $F_{preload}$ by measuring the kinetic friction on the substrate during the first 3 sec before the voltage is enabled and applying Eq. 17. We then solved Eq. 13 to predict the initial air gap before the voltage is enabled $T_{air}(t=0)$ and the final air gap after the voltage saturates $T_{air}(t \rightarrow \infty)$. The initial condition was set to $[T_{air}, \dot{T}_{air}] = [T_{air}(t=0), 0]$. The simulation was ended once the air gap traverses 0.5% of the way from $T_{air}(t=0)$ to $T_{air}(t \rightarrow \infty)$. This threshold was set by our ADC's effective noise-free number of bits at our sampling rate and gain, and corresponds to when we predict the ADC can first notice the force increasing on the load cell after the voltage is enabled.

B. Engagement Time Results and Discussion

Fig. 10 shows the engagement time across a total of 311 test runs over different drive voltages and frequencies, substrate widths, and preload forces, showing in general that the EA clutch can engage within several tens of microseconds. This matches our hypothesis when modeling that EA actuators can be designed to engage about as quickly as it takes to polarize their dielectric (for comparison, our power supply had a 10% - 90% rise time of 8.3 μ s, and our dielectric had a polarization relaxation time of $\tau = 2.82 \mu$ s). Across all 311 test runs, the average engagement time was 4.78 μ s ($\sigma = 7.07 \mu$ s), and 89.7% (279/311) of our measured engagement times were $<15 \mu$ s.

We observed significant run-to-run variance, which is not uncommon in the literature given the stochastic nature of the interaction between dielectric asperities and the substrate

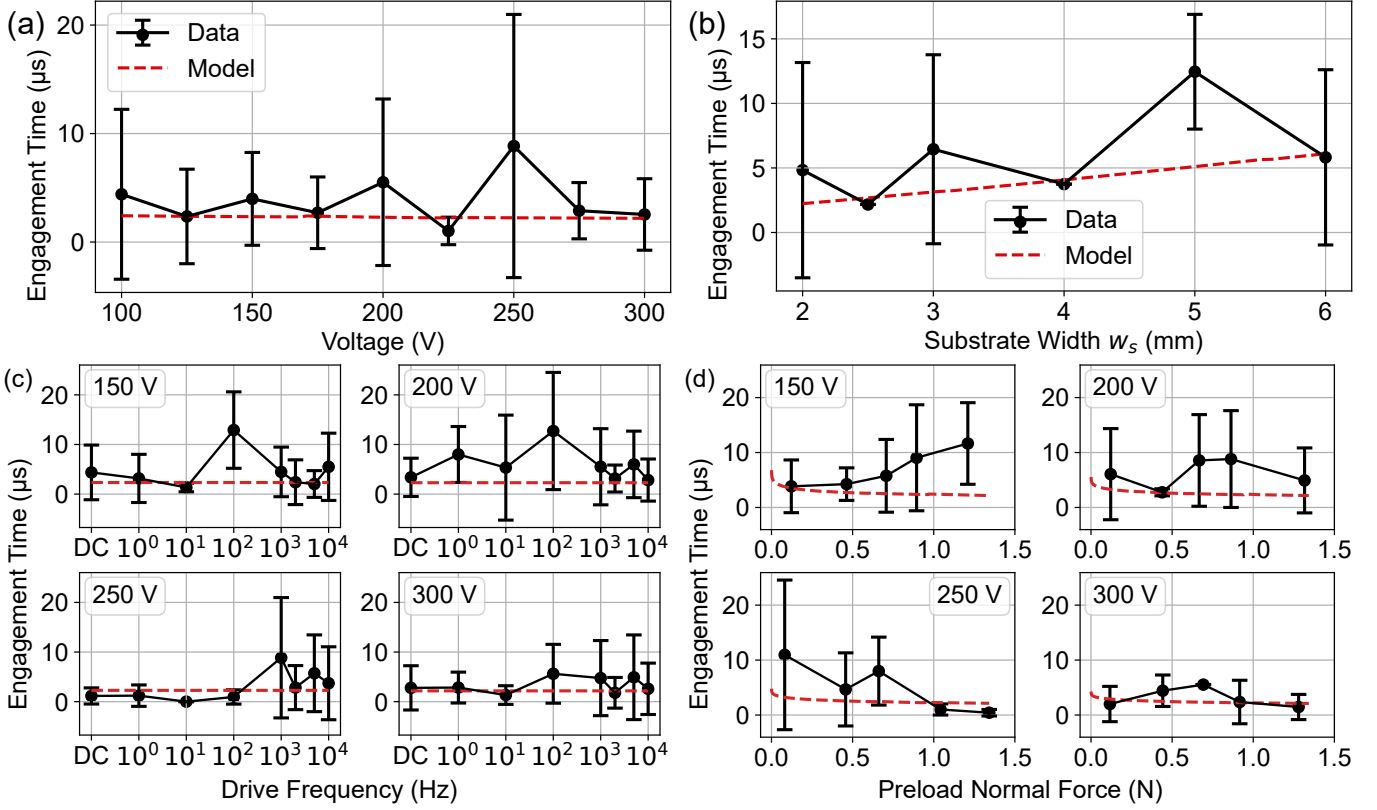


Fig. 10. Engagement time averaged over at least 4 trials per condition for different (a) voltages, (b) substrate widths, (c) drive frequencies, and (d) preload forces. Unless otherwise specified, the substrate width tested was 2 mm, the drive signal was a 300 V, 1 kHz bipolar square wave, and $F_{preload} < 0.25$ N.

[6, 8]. We also attribute this noise in part to our ADC. According to its datasheet, our ADC has 19.3 effective bits of resolution at our sample rate and gain, which allows our setup to detect force changes of about 125 μ N. At our experimental setup's movement speed (0.5 mm/s) and load cell spring constant ($k_{lc} = 18.0$ N/mm), this corresponds to a delay of about 13.9 μ s before we can expect to see a measurable change in force after the voltage engages. This aligns well with the range of standard deviations in our experimental results.

Comparing results for our 1.11–3.33 cm^2 EA-ICE clutches to prior literature, Hinchet and Shea [24] achieved engagement times of 5 ms for a 3 cm^2 parallel plate EA clutch, while Zhang et al. [8] achieved an engagement time of 6.7 ms for an 0.96 cm^2 EA-ICE clutch. In 1957, Fitch [25] achieved an engagement time of 150 μ s for a 38 cm^2 parallel plate rotary clutch using silicone oil as the dielectric and very precisely machined electrodes, which we believe helped reduce their interfacial surface roughness. While we are not able to directly apply our model to prior work, given our lack of contact models for their dielectric-substrate interfaces, we explore several hypotheses for why similarly sized EA clutches might see much larger engagement times in Sec. V.

Our model's predicted engagement times generally followed the trends of our experimental data. In Fig. 10(a), linearly interpolating the experimental data gives a similar slope -0.0013 $\mu\text{s}/\text{V}$ compared to our model's predicted slope -0.0012 $\mu\text{s}/\text{V}$. Both Diller et al. [6] and Zhang et al. [8] similarly observed that higher voltages corresponded to lower engagement

times. In Fig. 10(b), linearly interpolating the experimental data gives a slope 1.15 $\mu\text{s}/\text{mm}$ compared to our model's predicted slope 0.98 $\mu\text{s}/\text{mm}$. Notably, although the EA normal force is linearly proportional to the substrate width, we see a positive correlation between engagement time and substrate width instead of a negative one because the damping force scales as the cube of substrate width. In Fig. 10(c), as predicted by our model, we did not observe a consistent trend between engagement time and drive frequency because our measured engagement times were less than the period of any of our tested drive signals. In Fig. 10(d), our model predicted a small increase in engagement time for zero preload normal force, but it quickly steadied for higher preload forces, and we observed no consistent trend experimentally.

C. Release Time Testing and Simulation Methods

As shown in Fig. 6(c) and consistent with previous work [6, 24], we measured the release time for our EA clutches as the time between when the voltage begins to fall and when the load cell falls 90% of the way to its final steady-state value.

To simulate the release dynamics, in addition to the coupled equations of motion Eqs. 13 and 14 for T_{air} , we also modeled the load cell dynamics along the substrate's axis of motion:

$$m_{lc}\ddot{x}_{lc} = -k_{lc}x - b_{lc}\dot{x}_{lc} - F_{shear}\text{sign}(\dot{x}_{lc}) \quad (19)$$

where F_{shear} , given by Eq. 15, is calculated using static friction coefficients when $\dot{x} = 0$ and kinetic friction coefficients

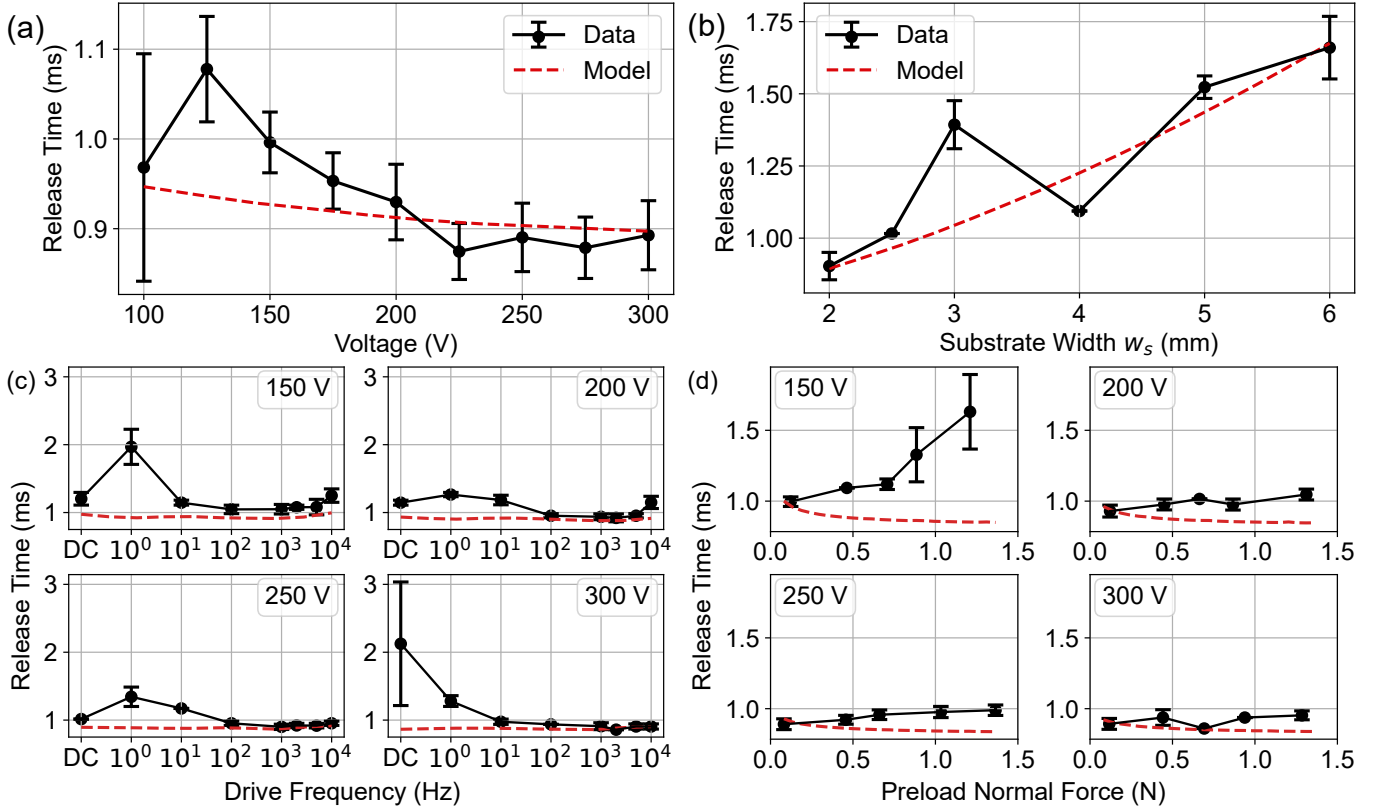


Fig. 11. Release time averaged over at least 4 trials per condition for different (a) voltages, (b) substrate widths, (c) drive frequencies, and (d) preload forces. Unless otherwise specified, the substrate width tested was 2 mm, the drive signal was a 300 V, 1 kHz bipolar square wave, and $F_{preload} < 0.25$ N.

otherwise. We measured the load cell's spring constant ($k_{lc} = 18.0$ N/mm), damping constant ($b_{lc} = 0.43 \frac{N \cdot s}{m}$), resonance frequency ($\omega_{lc} = 643.4$ Hz), and effective mass ($m_{lc} = 1.10$ g) by recording its response to step and ramp inputs to the load cell's position by the stepper motor. While the load cell dynamics were important to include in the model to fit the data, the load cell's quarter-period $\omega_{lc}/4 = 388.6 \mu s$ is small enough that we can expect the clutch's electromechanical dynamics to be the primary contributor to the measured release time.

For each experimental run, we estimated $F_{preload}$ by measuring the kinetic friction on the substrate during the first 3 sec before the voltage is enabled and applying Eq. 17. We also measured the ratio $\frac{F_{shear}(t_r)}{F_{shear,max}}$ between the load cell's applied force right before the voltage was released and the load cell's maximum measured force. Using $F_{preload}$, we solved the coupled equations of motion Eqs. 13 and 14 to calculate $T_{air}(t_r)$ at the moment of release. We then estimated the shear force capacity $F_{shear,max}^{predicted}$ of the EA pad using Eq. 16. We estimated the initial position of the load cell as:

$$x_{lc}(t_r) = \left(\frac{F_{shear,max}^{predicted}}{k_{lc}} \right) \left(\frac{F_{shear}(t_r)}{F_{shear,max}} \right) \quad (20)$$

where the second term on the right side is the value for each run, representing how far the load cell has stretched relative to its maximum displacement before the voltage released. The initial condition for the simulation is taken at the estimated

positions $T_{air}(t_r)$ and $x_{lc}(t_r)$ and with zero initial velocity. The simulation ends when the load cell returns to $x_{lc} = 0$.

D. Release Time Results and Discussion

Fig. 11 shows release time results for different geometric and operating parameters. The best release time was $874.6 \mu s$ ($\sigma = 31.2 \mu s$) for a 2 mm wide substrate, a low preload force (averaged over test runs with $F_{preload} < 0.25$ N), and a 225 V, 1 kHz drive signal. Across all 311 runs in our dataset, the average release time was 1.13 ms ($\sigma = 0.36$ ms), and 39.5% of the runs had release times < 1 ms.

Our release times are much faster than those in prior work. Hinchet and Shea [24] reported release times around 15 ms for a 3 cm² parallel plate clutch, while Diller et al. [45] measured 23.6 ms release times for a 80 cm² parallel plate clutch. The best EA-ICE clutch result we found was by Cao et al. [33], who measured release times of 100 ms for a 24.6 cm² clutch.

In Fig. 11(a), linearly interpolating the experimental data gives a slope $-0.72 \mu s/V$ compared to our model's predicted slope $-0.25 \mu s/V$. In Fig. 11(b), linearly interpolating the experimental data gives a similar slope $143.5 \mu s/mm$ compared to our model's predicted slope $142.3 \mu s/mm$. In prior work, Diller et al. [6] similarly observed that EA release times decrease with voltage and increase with substrate width.

In Fig. 11(c), we observed a local minima for release times, with 2 kHz drive frequencies causing on average 44.2% and 10.5% lower release times than 1 Hz and 10 kHz drive frequencies respectively. We did not find a model that captures

the low-frequency trend. Our original hypothesis was that our drive circuit might be leaking charge into the EA clutch, but Fig. 8 shows our clutch's shear force capacity did not increase at low frequencies. For drive frequencies above 2 kHz, however, our model did predict our experimental trend towards higher release times. At high frequencies, the EA force capacity decays, increasing the impact of slower mechanical dynamics in the release time. Notably, our experimental trends for release time line up very well with the trends in slip percentage from Fig. 9, where we saw the percentage of force lost after a slip decrease significantly as the drive frequency increased from 10 Hz to 2 kHz but increase slightly as the drive frequency increased to 10 kHz. We hypothesize that because our EA clutches can release faster around 2 kHz, at those drive frequencies it can also more quickly dissipate the interfacial static charges that accumulate after a slip and recover faster.

In Fig. 11(d), our model predicted that higher preload forces would cause lower release times, since as the preload force increases, the initial air gap is expected to decrease and the initial EA force is expected to increase. Because we initialized our load cell's position proportionally to $F_{shear,max}^{predicted}$, our model expected that the load cell would be initialized in a more deformed state, and thus that it would more quickly surpass static friction once the voltage is turned off. In practice, we measured larger release times at higher preload forces. We hypothesize the preload force caused our compliant dielectric film to wrap slightly around the substrate's edges, resulting in the EA pad also interfacing with the substrate's sidewalls.

V. SIMULATING PARAMETER SWEEPS FOR ENGAGEMENT AND RELEASE TIME

To inform future EA clutch designs, we extrapolated our dynamics model to plot its predicted engagement and release times across a wide range of design parameters.

Fig. 12 shows our model's predicted engagement time over different drive voltages, substrate widths and lengths, dielectric thicknesses, and drive circuit rise times. As shown, the substrate width, drive circuit rise time, and voltage all have very large effects on engagement time, while the dielectric thickness and substrate length have much smaller effects. The substrate's width affects engagement dynamics much more than its length does because the damping force increases as the cube of width but linearly with length. We also swept a variety of other parameters that did not have a large impact on the predicted engagement time, largely because our actuators engage so quickly that electrical and mechanical dynamics all change on a similar time scale. Our model predicted that the dielectric constant κ would have minimal effect on engagement time, because when the voltage first rises (i.e., when T_{air} is the largest) the κ^2 terms in the numerator and denominator of Eq. 4 roughly cancel out. The preload force also had little effect in our predicted and experimental results, which is promising for future work because we found a small preload significantly reduces wrinkling in the dielectric film.

Fig. 13 shows our model's predicted release time over the same design parameters. The substrate width matters the most for release time, followed by voltage and dielectric thickness.

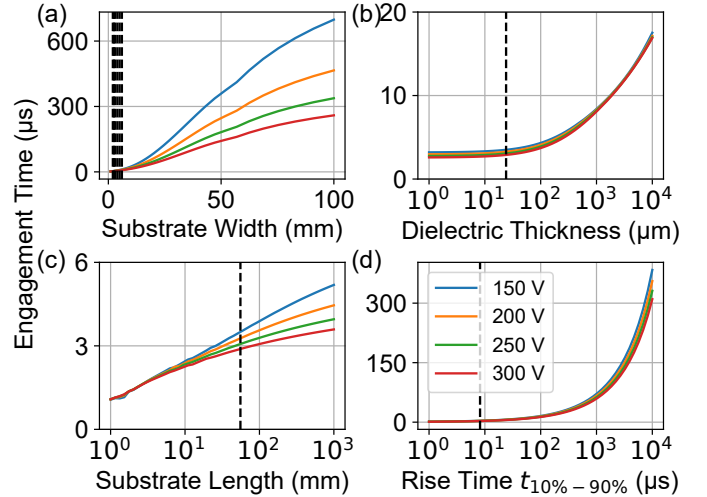


Fig. 12. Our model's predicted engagement time while varying voltage together with (a) substrate width, (b) dielectric thickness, (c) substrate length, and (d) the 10% - 90% rise time of our high voltage drive circuit. The black dotted lines indicate the values tested in this paper. Unless otherwise specified, the substrate width tested was 2 mm, the drive signal was a 300 V, 1 kHz bipolar square wave, and $F_{preload} = 0.125$ N.

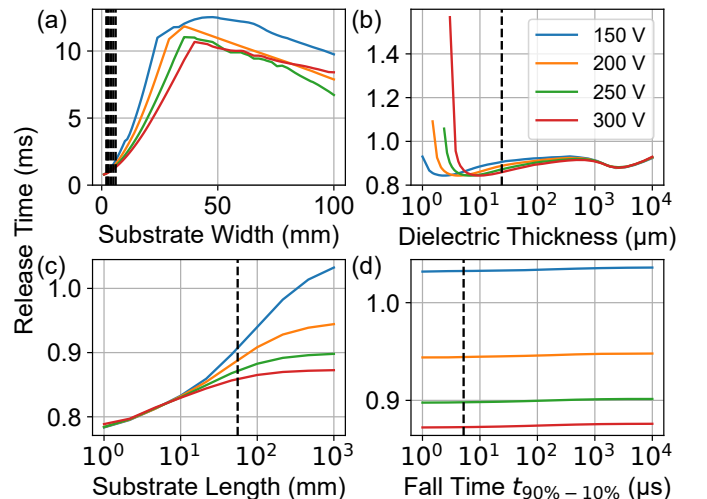


Fig. 13. Our model's predicted release time while varying voltage together with (a) substrate width, (b) dielectric thickness, (c) substrate length, and (d) the 90% - 10% fall time of our high voltage drive circuit. The black dotted lines indicate the values tested in this paper. Unless otherwise specified, the substrate width tested was 2 mm, the drive signal was a 300 V, 1 kHz bipolar square wave, $F_{preload} = 0.125$ N, and $F_{shear}(t_r)/F_{shear,max} = 0.8$.

For larger substrate widths, after the rate of increase in our contact force $F_k(T_{air})$ at small air gaps outpaces that of our EA force $F_{ea}(T_{air})$, larger substrate widths are predicted by our model to see lower release times. The dielectric thickness has an interesting local minima in its graph as the dielectric's increasing mass compensates for the loss of EA force capacity when determining the initial air gap before release. Diller et al. [6] similarly observed higher release times at larger substrate widths and lengths, lower voltages, and in an intermediate dielectric thickness range for parallel plate EA clutches, but to our knowledge this is the first time these trends have been replicated by a physics-based model. The high voltage

drive circuitry's fall time only has a small positive correlation with release time, as it slightly delays when the load cell can overcome static friction and because slower mechanical dynamics predominantly influence the release time.

These simulations help establish important design tradeoffs for EA clutches. Because the electroadhesive force is proportional to substrate area, long, narrow EA clutches can achieve much faster engagement and release times while achieving the same force capacity. Diller et al. [6] discovered a similar principle experimentally, when they found that cutting slits into a large EA pad significantly improved release time without harming shear force capacity, and we expect future timing-focused clutch designs will further explore the design space. Improved dynamics also result in faster recovery after slip, opening new uses for EA clutches in applications requiring robustness. The high voltage drive circuit's rise time also makes a big difference in an EA clutch's engagement time, which can motivate important decisions over the choice of high voltage amplifier and output stage needed for a project.

VI. CONCLUSIONS AND FUTURE WORK

In this paper, we developed a dynamics model for EA-ICE clutches loaded in shear against metallic substrates. As a part of this model, we presented a simple calibration procedure to estimate the interfacial contact mechanics between the dielectric and substrate, bypassing the time and machine cost associated with traditional surface profilometry. We also integrated a dielectric polarization model, proposing that dielectrics can be charged and discharged within microseconds rather than the seconds to minutes commonly assumed in prior modeling work. We then experimentally measured EA shear force capacity, engagement time, and release time over a variety of device parameters and compared our experimental trends to our model's predictions with good conformity.

We conclude that the drive frequency, voltage, and substrate width to length aspect ratio significantly impact EA engagement and release times. While previous clutches in the literature have focused on square or circular patterns at low drive frequencies (DC or ≤ 10 Hz AC), our simulations and experimental results show that longer, narrower clutches at higher drive frequencies can provide a better trade-off between shear force capacity and actuation time. In our setup, 1-2 kHz drive frequencies achieved the highest shear force capacities, lowest release times, and best slip recoveries, but we expect this optimal range will vary for each EA clutch design.

Our current work has some drawbacks, most notably in its simplified contact mechanics model and handling of parasitics. Future work should investigate more advanced contact models, integrating the substrate's surface energy and work function to understand what happens at the transition between frictional and peeling fracture mechanics and how the stochastic interactions between local asperities translates to the global shear force. Our model also assumed that the substrate is a metal, in which charges can be induced much faster than in an insulating substrate. Future work should investigate faster and more precise tools to measure the engagement and release times across a variety of substrates.

We believe that improving the dynamics of electroadhesion opens new potential for high-bandwidth soft robots and haptic user interfaces. EA clutches have already received attention among switchable adhesives for their low power, low cost, low mass, and scalable manufacturing processes. However, while micro-electromechanical systems have leveraged these advantages to create kHz-driven precision electrostatic actuators for centimeter-scale rockets and grippers [46, 47], existing soft actuators generally operate under orders of magnitude less accuracy and speed [13]. Similarly, existing EA integrations into haptic user interfaces have historically faced limited bandwidth, with -3 dB frequencies on the order of tens to hundreds of Hertz [10, 23]. By understanding more about how different geometric and operating parameters affect electroadhesion's response speed, we believe it can become a versatile, space- and power-efficient actuator for future robots.

ACKNOWLEDGMENTS

The authors thank Wing-Sum A. Law, Savannah Cofer, Danyang Fan, and Olivia Tomassetti for providing feedback on this paper.

REFERENCES

- [1] V. Cacucciolo, H. Shea, and G. Carbone, "Peeling in electroadhesion soft grippers," *Extreme Mechanics Letters*, vol. 50, p. 101529, Jan. 2022.
- [2] M. Mastrangelo, F. Caruso, G. Carbone, and V. Cacucciolo, "Electroadhesion zipping with soft grippers on curved objects," *Extreme Mechanics Letters*, vol. 61, p. 101999, Jun. 2023.
- [3] S. Park, D. S. Drew, S. Follmer, and J. Rivas-Davila, "Lightweight high voltage generator for untethered electroadhesive perching of micro air vehicles," *IEEE Robotics and Automation Letters*, vol. 5, no. 3, p. 4485–4492, Jul. 2020.
- [4] M. A. Graule, P. Chirattananon, S. B. Fuller, N. T. Jafferis, K. Y. Ma, M. Spenko, R. Kornbluh, and R. J. Wood, "Perching and takeoff of a robotic insect on overhangs using switchable electrostatic adhesion," *Science*, vol. 352, no. 6288, p. 978–982, May 2016.
- [5] E. Krimsky and S. H. Collins, "Elastic energy-recycling actuators for efficient robots," *Science Robotics*, vol. 9, no. 88, p. eadj7246, Mar. 2024.
- [6] S. B. Diller, S. H. Collins, and C. Majidi, "The effects of electroadhesive clutch design parameters on performance characteristics," *Journal of Intelligent Material Systems and Structures*, vol. 29, no. 19, p. 3804–3828, Nov. 2018.
- [7] A. M. Rauf, J. S. Bernardo, and S. Follmer, "Electroadhesive auxetics as programmable layer jamming skins for formable crust shape displays," in *IEEE International Conference on Robotics and Automation (ICRA)*, May 2023, p. 2591–2597.
- [8] K. Zhang, E. J. Gonzalez, J. Guo, and S. Follmer, "Design and analysis of high-resolution electrostatic adhesive brakes towards static refreshable 2.5d tactile shape display," *IEEE Transactions on Haptics*, vol. 12, no. 4, p. 470–482, Oct. 2019.
- [9] D. Leithinger, R. Zhou, E. Acome, A. M. Rauf, T. Han, C. Shultz, and J. Mullenbach, "Electro-actuated materials for future haptic interfaces," in *Adjunct ACM Symposium on User Interface Software and Technology*, Oct. 2023, p. 1–3.
- [10] C. Shultz, M. Peshkin, and J. E. Colgate, "The application of tactile, audible, and ultrasonic forces to human fingertips using broadband electroadhesion," *IEEE Transactions on Haptics*, vol. 11, no. 2, p. 279–290, Apr. 2018.
- [11] V. Vechev, R. Hinchet, S. Coros, B. Thomaszewski, and O. Hilliges, "Computational design of active kinesthetic garments," *ACM Symposium on User Interface Software and Technology*, p. 1–11, Oct. 2022.
- [12] R. J. Hinchet and H. Shea, "Glove- and sleeve-format variable-friction electrostatic clutches for kinesthetic haptics," *Advanced Intelligent Systems*, vol. 4, no. 12, p. 2200174, 2022.
- [13] A. B. Croll, N. Hosseini, and M. D. Bartlett, "Switchable adhesives for multifunctional interfaces," *Advanced Materials Technologies*, vol. 4, no. 8, p. 1900193, 2019.

- [14] J. Wang and A. Chortos, "Control strategies for soft robot systems," *Advanced Intelligent Systems*, vol. 4, no. 5, p. 2100165, 2022.
- [15] A. K. Han, A. Hajji-Ahmad, and M. R. Cutkosky, "Hybrid electrostatic and gecko-inspired gripping pads for manipulating bulky, non-smooth items," *Smart Materials and Structures*, vol. 30, no. 2, p. 025010, Dec. 2020.
- [16] R. P. Krape, *Applications study of electroadhesive devices*, Oct. 1968, no. NASA-CR-1211.
- [17] Y. Wang, S.-G. Lu, M. Lanagan, and Q. Zhang, "Dielectric relaxation of relaxor ferroelectric p(vdf-trfe-cfe) terpolymer over broad frequency range," *IEEE Transactions on Ultrasonics, Ferroelectrics, and Frequency Control*, vol. 56, no. 3, p. 444–449, Mar. 2009.
- [18] H. Tang, Y. Lin, and H. A. Sodano, "Ultra high energy density nanocomposite capacitors using surface-functionalized batio₃ nanowires and pvdF-trfe-cfe," in *Behavior and Mechanics of Multifunctional Materials and Composites*, vol. 8342. SPIE, Mar. 2012, p. 33–40.
- [19] R. Chen, F. Liu, H. Wang, X. Zhu, X. Tao, S. Zhang, and G. Jiang, "Theoretical and experimental analyses of the dynamic electroadhesion force," *Extreme Mechanics Letters*, vol. 56, p. 101892, Oct. 2022.
- [20] T. Nakamura and A. Yamamoto, "Modeling and control of electroadhesion force in dc voltage," *ROBOMECH*, vol. 4, no. 1, p. 18, Jun. 2017.
- [21] R. Chen, Z. Zhang, R. Song, C. Fang, D. Sindesberger, G. J. Monkman, and J. Guo, "Time-dependent electroadhesive force degradation," *Smart Materials and Structures*, vol. 29, no. 5, p. 055009, Mar. 2020.
- [22] P. Rajagopalan, M. Muthu, Y. Liu, J. Luo, X. Wang, and C. Wan, "Advancement of electroadhesion technology for intelligent and self-reliant robotic applications," *Advanced Intelligent Systems*, vol. 4, no. 7, p. 2200064, 2022.
- [23] E. Leroy and H. Shea, "Hydraulically amplified electrostatic taxels (haxels) for full body haptics," *Advanced Materials Technologies*, vol. 8, no. 16, p. 2300242, 2023.
- [24] R. Hinchet and H. Shea, "High force density textile electrostatic clutch," *Advanced Materials Technologies*, vol. 5, no. 4, p. 1900895, 2020.
- [25] C. J. Fitch, "Development of the electrostatic clutch," *IBM Journal of Research and Development*, vol. 1, no. 1, p. 49–56, Jan. 1957.
- [26] J. Jeon and T. Higuchi, "Electrostatic suspension of dielectrics," *Transactions on Industrial Electronics*, vol. 45, no. 6, p. 938–946, Dec. 1998.
- [27] X. Gao, C. Cao, J. Guo, and A. Conn, "Elastic electroadhesion with rapid release by integrated resonant vibration," *Advanced Materials Technologies*, vol. 4, no. 1, p. 1800378, 2019.
- [28] X. Q. Chen and M. Sarhadi, "Investigation of electrostatic force for robotic lay-up of composite fabrics," *Mechatronics*, vol. 2, no. 4, p. 363–373, Aug. 1992.
- [29] R. Thilakarathna and M. Phlernjai, "Design and development of a lightweight, low-cost cylindrical electrostatic clutch," *Engineering Science and Technology, an International Journal*, vol. 49, p. 101600, Jan. 2024.
- [30] J. Li, "Electroadhesive clutches made from high dielectric-constant polymeric materials and flexible electrodes," Ph.D. Dissertation, Hong Kong Polytechnic University, 2021.
- [31] V. Cacucciolo, J. Shintake, and H. Shea, "Delicate yet strong: Characterizing the electro-adhesion lifting force with a soft gripper," *IEEE International Conference on Soft Robotics*, p. 108–113, Apr. 2019.
- [32] Z. Yoder, D. Macari, G. Kleinwaks, I. Schmidt, E. Acome, and C. Keplinger, "A soft, fast and versatile electrohydraulic gripper with capacitive object size detection," *Advanced Functional Materials*, vol. 33, no. 3, p. 2209080, 2023.
- [33] C. Cao, X. Gao, J. Guo, and A. Conn, "De-electroadhesion of flexible and lightweight materials: An experimental study," *Applied Sciences*, vol. 9, no. 1414, p. 2796, Jan. 2019.
- [34] D. Wei, Q. Xiong, J. Dong, H. Wang, X. Liang, S. Tang, X. Xu, H. Wang, and H. Wang, "Electrostatic adhesion clutch with superhigh force density achieved by mxene-poly(vinylidene fluoride-trifluoroethylene-chlorotrifluoroethylene) composites," *Soft Robotics*, vol. 10, no. 3, p. 482–492, Jun. 2023.
- [35] J. Li, Y. Xiong, K. Ma, B. Yang, L. Ma, and X. Tao, "Asymmetric strategy for enhanced performance of flexible electroadhesive clutch," *Heliyon*, vol. 9, no. 2, Feb. 2023.
- [36] A. S. Chen and S. Bergbreiter, "A comparison of critical shear force in low-voltage, all-polymer electroadhesives to a basic friction model," *Smart Materials and Structures*, vol. 26, no. 2, p. 025028, Jan. 2017.
- [37] N. Berdozzi, Y. Chen, L. Luzi, M. Fontana, I. Fassi, L. Molinari Tosatti, and R. Vertechy, "Rapid fabrication of electro-adhesive devices with inkjet printed electrodes," *IEEE Robotics and Automation Letters*, vol. 5, no. 2, p. 2770–2776, Apr. 2020.
- [38] C. Shultz and C. Harrison, "Flat panel haptics: Embedded electroosmotic pumps for scalable shape displays," in *Conference on Human Factors in Computing Systems*, Apr. 2023, p. 1–16.
- [39] V. Ramachandran, J. Shintake, and D. Floreano, "All-fabric wearable electroadhesive clutch," *Advanced Materials Technologies*, vol. 4, no. 2, p. 1800313, 2019.
- [40] D. J. Levine, K. T. Turner, and J. H. Pikul, "Materials with electroprogrammable stiffness," *Advanced Materials*, vol. 33, no. 35, p. 2007952, 2021.
- [41] J. A. Greenwood and J. B. P. Williamson, "Contact of nominally flat surfaces," *Proceedings of the Royal Society of London. Series A, Mathematical and Physical Sciences*, vol. 295, no. 1442, p. 300–319, 1966.
- [42] W. S. Griffin, H. H. Richardson, and S. Yamanami, "A study of fluid squeeze-film damping," *Journal of Basic Engineering*, vol. 88, no. 2, p. 451–456, Jun. 1966.
- [43] M. Ayyildiz, M. Scaraggi, O. Sirin, C. Basdogan, and B. N. J. Persson, "Contact mechanics between the human finger and a touchscreen under electroadhesion," *Proceedings of the National Academy of Sciences*, vol. 115, no. 50, p. 12668–12673, Dec. 2018.
- [44] S. Schaller and H. Shea, "Measuring electro-adhesion pressure before and after contact," *Scientific Reports*, vol. 13, no. 1, p. 11768, Jul. 2023.
- [45] S. Diller, C. Majidi, and S. H. Collins, "A lightweight, low-power electroadhesive clutch and spring for exoskeleton actuation," in *International Conference on Robotics and Automation*, May 2016, p. 682–689.
- [46] A. M. Rauf, D. S. Contreras, R. M. Shih, C. B. Schindler, and K. S. J. Pister, "Nonlinear dynamics of lateral electrostatic gap closing actuators for applications in inchworm motors," *Journal of Microelectromechanical Systems*, vol. 31, no. 1, p. 29–36, Feb. 2022.
- [47] A. M. Rauf, B. G. Kilberg, C. B. Schindler, S. A. Park, and K. S. J. Pister, "Towards aerodynamic control of miniature rockets with mems control surfaces," in *IEEE Conference on Micro Electro Mechanical Systems (MEMS)*, Jan. 2020, p. 523–526.



Ahad M. Rauf (Graduate Student Member, IEEE) received the B.S. degree in electrical engineering and computer sciences from the University of California at Berkeley, CA, USA, and the M.S. degree in mechanical engineering in 2022 from Stanford University, Stanford, CA, USA, where he is currently working towards the Ph.D. degree in mechanical engineering.

His research interests include compliant mechanisms, variable stiffness structures, and soft robotics.



Sean Follmer (Member, IEEE) received the B.S. degree in engineering, with a focus on product design, from Stanford University, Stanford, CA, USA, in 2009, and the M.S. and Ph.D. degrees in human-computer interaction from MIT Media Laboratory, Cambridge, MA, USA, in 2011 and 2015, respectively. He is currently an Associate Professor of Mechanical Engineering and Computer Science (by courtesy) with Stanford University. He also directs the Stanford SHAPE Laboratory and is a member of the Stanford HCI Group.